Tecnociencia, Vol. 28, N°2: 184-209
Julio-Diciembre 2026
ISSN L 2415-0940

Green precursor-assisted solid-state synthesis of $LaFeO_3$ perovskite: role of tannic acid on structural and magnetic properties

Síntesis en estado sólido de perovskita LaFeO3 asistida por precursor verde: papel del ácido tánico en las propiedades estructurales y magnéticas

Fernando J. Higuera
Universidad de Panamá, Departamento de Física, Panamá
fernando-j.higuera@up.ac.pa https://orcid.org/0009-0009-0407-4721

Juan A. Jaén
Universidad de Panamá, Departamento de Química, Panamá.
juan.jaen@up.ac.pa https://orcid.org/0000-0001-7069-216X

Fecha de recepción: 8 de enero de 2026
Fecha de aceptación: 11 de mayo de 2026

DOI: https://doi.org/10.48204/j.tecno.v8n2.a10869

ABSTRACT

$LaFeO_3$ was synthesized via a low-energy solid-state route using commercial and tannic-acid-derived hematite as Fe precursors under identical processing (8 h milling + calcination at 800°C for 20 h, followed by 5 h post-milling), producing four samples. XRD confirms predominantly orthorhombic $LaFeO_3$ (Pnma) in all cases, with residual hematite; the green-precursor samples show lower conversion and minor residual La_2O_3. Post-milling induces crystallite refinement and increased microstrain in all samples, with the green-precursor material exhibiting smaller crystallites (≈ 79 nm vs ≈ 91 nm) and more pronounced microstrain, reflecting its initially heterogeneous reaction pathway. Mössbauer spectroscopy shows a single $LaFeO_3$ sextet, with reduced intensity in the green-precursor samples, consistent with residual non-reacted regions. FTIR and XPS reveal organic-derived species only in these samples, while SEM shows agglomerated micrometric structures of nanosized particles, slightly smaller on average. Room-temperature M–H curves confirm weak ferromagnetic behavior, and ZFC–FC measurements display features associated with minor hematite and strong thermal irreversibility, attributed to uncompensated spins enhanced by milling.

KEYWORDS

$LaFeO_3$; Solid-state synthesis; Low-energy ball milling; Tannic acid; Mössbauer spectroscopy

RESUMEN

Se sintetizo $LaFeO_3$ mediante una ruta de estado sólido de baja energía utilizando hematita comercial y hematita derivada de ácido tánico como precursores de Fe bajo el mismo procesamiento (8 h de molienda + calcinación a 800 °C durante 20 h, seguido de 5 h de post-molienda), produciendo cuatro muestras. La difracción de rayos X (XRD) confirma la presencia predominante de $LaFeO_3$ ortorrómbico (Pnma) en todos los casos, con hematita residual; las muestras del precursor verde muestran una menor conversión y una pequeña cantidad de La2O3 residual. La post-molienda induce el refinamiento de los cristalitos y un aumento de la microdeformación en todas las muestras, donde el material del precursor verde exhibe cristalitos más pequeños (≈ 79 nm frente a ≈ 91 nm) y una microdeformación más pronunciada, lo que refleja su vía de reacción inicialmente heterogénea. La espectroscopia Mössbauer muestra un único sextete de $LaFeO_3$, con una intensidad reducida en las muestras del precursor verde, lo cual es consistente con las regiones residuales no reaccionadas. Las técnicas FTIR y XPS revelan especies derivadas de compuestos orgánicos solo en estas muestras, mientras que la microscopía electrónica de barrido (SEM) muestra estructuras micrométricas aglomeradas de partículas nanométricas, ligeramente más pequeñas en promedio. Las curvas M-H a temperatura ambiente confirman un comportamiento ferromagnético débil, y las mediciones ZFC-FC muestran características asociadas con la hematita minoritaria y una fuerte irreversibilidad térmica, atribuida a espines no compensados potenciados por la molienda.

PALABRAS CLAVE

$LaFeO_3$; Síntesis en estado sólido; Molienda de bolas de baja energía; Ácido tánico; Espectroscopia Mössbauer.

INTRODUCTION

A notable characteristic of this compound is that its functional properties depend strongly on the synthesis route (Koferstein et al., 2013; Kucharczyk et al., 2020; Ozkan et al., 2020; Popa & Moreno, 2010). Reported optical band gaps vary between 2.1 and 3.85 eV (Koferstein et al., 2013), specific surface areas from 2 to 30 m^2/g (Keav et al., 2014), and coercive fields from 853 Oe to 32 kOe (Koferstein et al., 2013; Naibaho et al., 2024; Prasad et al., 2024). Such wide ranges reflect differences in precursor chemistry and reaction pathways, arising from the large number of synthesis methods that have been studied for this compound, namely, sol–gel (Azouzi et al., 2019; Lebid & Omari, 2014; Ozkan et al., 2020), co-precipitation (Jadhav et al., 2006), and solid-state routes (Berbenni et al., 2018; Cristóbal et al., 2009; Lugo et al., 2021; Sorescu et al., 2011).

In parallel, the increasing demand for nanostructured oxides has intensified interest in synthesis routes that are more environmentally sustainable (Ahmad, 2014; Pasieczna-Patkowska et al., 2025). Many conventional physicochemical methods rely on high energy consumption or on organic solvents and chemical additives that may be difficult to handle and generate environmentally persistent residues (Pasieczna-Patkowska et al., 2025). In this context, plant-derived compounds have emerged as attractive alternatives, as they can act

simultaneously as chelating and reducing agents, potentially reducing both environmental impact and synthesis complexity (Herrera-Becerra et al., 2010; Pasieczna-Patkowska et al., 2025).

Among these bio-based precursors, tannic acid (TA), a plant polyphenolic compound capable of coordinating metal cations and promoting the formation of polymeric metal–organic networks, is particularly promising (Ahmad, 2014; Herrera-Becerra et al., 2010). It has already been employed in the synthesis of metallic and oxide nanoparticles, where it can influence reaction temperature and crystallite size by modifying nucleation and growth conditions (Ahmad, 2014; Finlay et al., 2012; Freire et al., 2023; Herrera-Becerra et al., 2010). However, despite its demonstrated utility in oxide synthesis, its effect on the formation pathway, resulting microstructure, and functional properties of $LaFeO_3$ remains largely unexplored.

In this work, we address this gap by combining a bio-derived iron precursor with a mild physical processing step. Hematite synthesized using tannic acid is employed as the Fe source, and a low-energy ball-milling treatment is introduced before calcination to homogenize the reagents while minimizing energy input. By comparing $LaFeO_3$ produced from tannic acid-derived hematite with that obtained from commercial hematite under identical processing conditions, we assess the impact of the bio-based precursor on phase formation, microstructure, and magnetic response, and evaluate its potential as a more sustainable route for $LaFeO_3$ synthesis

METHODOLOGY

Materials

Iron(III) nitrate nonahydrate ($Fe(NO_3)_3 \cdot 9H_2O$, 98%, Sigma-Aldrich) was used as the iron precursor. Tannic acid (CAS 1401-55-4, from Chinese natural gall nuts, Sigma-Aldrich) was employed as a complexing agent. Sodium hydroxide (NaOH, pellets, ≥98%, Merck Emplura) was used to adjust pH.

Commercial hematite (Fe_2O_3, 97%, 25 μm, Panreac Applichem) and lanthanum oxide (La_2O_3, 99.5%, 25 μm, Merck Emplura) were used for solid-state synthesis.

Synthesis of $LaFeO_3$

The green precursor was produced following (Freire, et al, 2023) by dissolving $Fe(NO_3)_3 \cdot 9H_2O$ in water (10 wt%), mixing it with a 0.1 wt% tannic acid solution, and stirring for 24 h to allow full complexation. The pH was then adjusted to 5 using NaOH solution (0.2 M), and the resulting precipitate was washed repeatedly by centrifugation to remove Na^+. After drying for 15 h, the solid was calcined at 700 °C for 3 h, yielding Fe_2O3 nanoparticles.

Both this precursor and commercial hematite were used to synthesize $LaFeO_3$ under identical solid-state conditions. Equimolar amounts of hematite and La_2O_3 were ball-milled in a planetary mill (FRITSCH Pulverisette 5) with methanol as dispersant and a 12:1 ball-to-powder mass ratio.

The milling and calcination parameters employed were established through a systematic optimization study previously conducted by our group, in which different milling durations and thermal treatments were evaluated while keeping the milling conditions (rotational speed, milling medium, and ball-to-powder ratio) fixed. These tests showed that 8 h of wet milling, followed by calcination at 800 °C for 20 h, yielded the highest $LaFeO_3$ phase fraction. The corresponding optimization study has been previously reported in detail (Jaén et al., 2026).

After calcination, all samples underwent an additional 5 h of dry milling under the same milling conditions to mitigate potential sintering and improve homogeneity. The resulting samples were labeled according to the precursor used and the application of the post-calcination milling step: ATLFO and ATLFO5 for samples obtained from tannic acid-derived hematite, and LFO and LFO5 for those synthesized from commercial hematite.

Characterization techniques

X-ray diffraction (XRD) patterns were collected using a Malvern Panalytical Aeris diffractometer equipped with a Co–Kα source and a goniometer-type scanner. Data were acquired from 10° to 100° (2θ) with a step size of 0.022°. Phase identification was performed using HighScore Plus and the COD and PDF-2 databases, and quantitative analysis was carried out by Rietveld refinement in the same software.

FTIR spectra of ATLFO5 were acquired in transmission mode using a PerkinElmer Spectrum Two spectrometer (resolution: 0.2 cm^{-1}, 4000–400 cm^{-1}). The FTIR spectrum of LFO5 was obtained in ATR mode using a PerkinElmer Frontier system (resolution: 2 cm^{-1}, 4000–300 cm^{-1}). Atmospheric corrections were applied in both cases.

SEM images were obtained using a Thermo Scientific Quattro microscope (Thermo Fisher) operated in high vacuum. Both ETD and CBS detectors were used to record topographical and compositional contrast, respectively. Acceleration voltages of 10–20 kV, a spot size of 3, and a working distance of 4.8–4.9 mm were employed.

XPS spectra were recorded using a Specs NAP-XPS system with a PHOIBOS 150 1D-DLD analyzer and a monochromatic Al–Kα source (1486.7 eV, 13 kV, 100 W). Survey spectra were collected with a 1 eV pass energy, and high-resolution spectra with 0.1 eV. A 3 eV, 20 μA charge neutralization was applied. Data processing was performed with CasaXPS.

Room-temperature Mössbauer spectra were collected using a CTS4 spectrometer (constant acceleration mode, 1024 channels) with a ^{57}Co/Rh source. Samples were prepared as 13 mm pellets containing 30–70 mg of powder diluted in sucrose. Velocity calibration was performed relative to α-Fe. Hyperfine parameters were obtained using Recoil.

Magnetic measurements were carried out using a PPMS system (Quantum Design) with a VSM head. M–H loops were recorded at 300 K under vacuum (26 Torr) in an applied field of ±20 kOe. M–T curves were acquired under ZFC and FC protocols from 5 to 300 K with an applied field of 200 Oe.

RESULTS

Structural analysis

XRD analysis

XRD measurements were carried out to evaluate the crystalline phases and structural features of the samples. Both the calcined and post-milled powders were analyzed. However, since the post-milled powders represent the final processed state for each synthesis route, most of the discussion focuses on LFO5 and ATLFO5. It should be noted that all diffraction patterns presented were normalized for visualization purposes; therefore, peak intensities are not directly comparable between samples.

The diffraction patterns of samples ATLFO and LFO are shown in Figure 1, and their corresponding refined parameters are listed in Table 1. Both samples crystallize predominantly in orthorhombic $LaFeO_3$ (Pnma, COD 1561805), exhibiting nearly identical lattice constants, cell volumes, and microstrain values, in agreement with the literature (Saha et al., 2020; Morales et al., 2016). The main difference between the two lies in phase purity: ATLFO contains 92.7% $LaFeO_3$ and retains measurable La_2O_3, whereas LFO reaches 96.8% purity with no detectable lanthanum oxide.

Figure 1

Experimental diffraction pattern (black), fit (red), and identified phases in samples (a) ATLFO and (b) LFO.

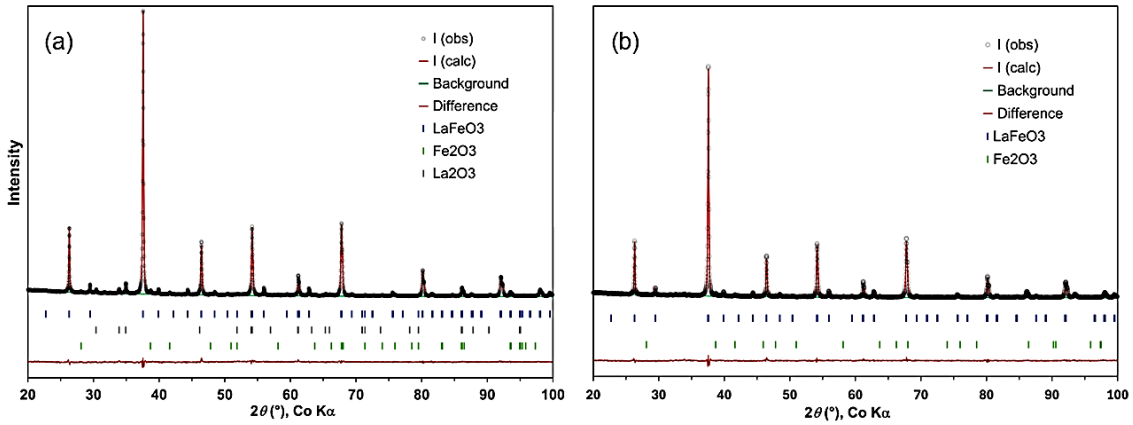

Table 1

Parameters derived from Rietveld analysis in samples ATLFO and LFO.

ATLFO				LFO		
Parameter	**$LaFeO_3$**	**Fe_2O_3**	**La_2O_3**	**Parameter**	**$LaFeO_3$**	**Fe_2O_3**
a (Å)	5.5622(2)	5.036(2)	3.9394(8)	a (Å)	5.5638(2)	5.034(2)
b (Å)	7.8547(2)	5.036(2)	3.9394(8)	b (Å)	7.8546(2)	5.034(2)
c (Å)	5.5565(2)	13.743(6)	6.134(1)	c (Å)	5.5558(2)	13.753(6)
Volume ($Å^3$)	242.76(9)	-	-	Volume ($Å^3$)	242.799(9)	–
Phase %	92.7(1)	3.8(1)	3.5(3)	Phase %	96.8(5)	3.2(3)
Crystallite size (nm)	97(3)	–	–	Crystallite size (nm)	100(4)	–
Microstrain (%)	0.029(8)	–	–	Microstrain (%)	0.030(7)	–

The lower conversion in ATLFO is likely associated with the hematite precursor obtained from TA. Previous studies have shown that materials produced from this organic compound may retain carbonaceous surface residues (Finlay et al., 2012; Freire et al., 2023), which can hinder cation diffusion during calcination. Reduced ionic mobility would slow the formation of $LaFeO_3$, promoting the persistence of unreacted La_2O_3.

The diffraction patterns of the additional milled samples are shown in Figure 2, and their corresponding refined parameters are listed in Table 2.

Figure 2

Experimental diffraction pattern (black), fit (red), and identified phases in samples (a) ATLFO5 and (b) LFO5.

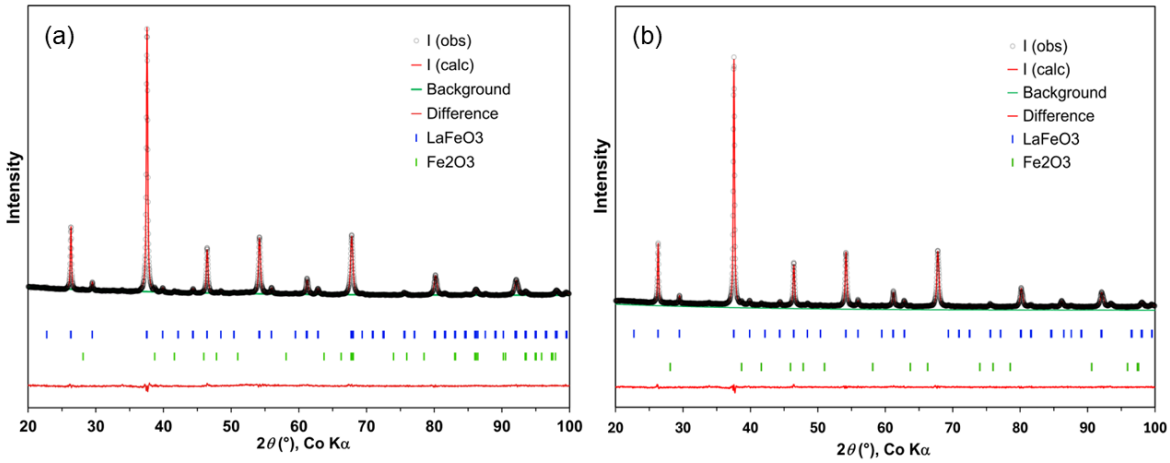

In both samples, milling increases microstrain without significantly altering lattice parameters or cell volume, indicating that the unit cell remains structurally stable. However, the effect of post-calcination milling is different. Although LFO5 shows only a moderate reduction in crystallite size and increased strain, ATLFO5 exhibits a significantly smaller crystallite size (≈ 79 nm) compared to LFO5 (≈ 91 nm) and a higher microstrain (≈ 0.125%). This indicates that the $LaFeO_3$ obtained from hematite derived from TA is structurally more susceptible to mechanical refinement, which may be linked to the presence of precursor phases after calcination, resulting in a more heterogeneous, multiphasic microstructure with numerous internal interfaces that could act as weak mechanical regions during milling.

Table 2

Parameters derived from Rietveld analysis in samples ATLFO5 and LFO5

ATLFO5			LFO5		
Parameter	**$LaFeO_3$**	**Fe_2O_3**	**Parameter**	**$LaFeO_3$**	**Fe_2O_3**
a (Å)	5.5654(5)	5.036(3)	a (Å)	5.5622(4)	5.034(2)
b (Å)	7.8529(5)	5.036(3)	b (Å)	7.8553(5)	5.034(2)
c (Å)	5.5571(4)	13.75(1)	c (Å)	5.5561(3)	13.753(6)
Volume ($Å^3$)	242.87(2)	-	Volume ($Å^3$)	242.76(2)	–
Phase %	97.8(2)	2.2(1)	Phase %	97.6(1)	2.4(3)
Crystallite size (nm)	79(3)	–	Crystallite size (nm)	91.1(4)	–
Microstrain (%)	0.125(4)	–	Microstrain (%)	0.108(7)	–

In ATLFO5, the reflections associated with La_2O_3 disappear, but the overall peak intensity decreases noticeably, as shown in Figure 3.

Figure 3
Diffraction patterns of samples ATLFO (black) and ATLFO5 (red).

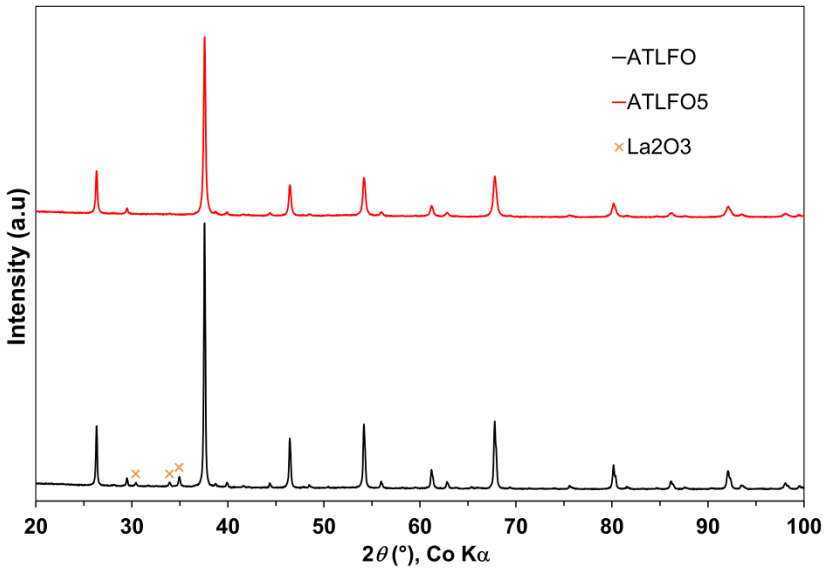

The milling conditions used here are far below the energies required for mechanochemical synthesis using bulk precursors (Cherkezova-Zheleva et al., 2014; Sorescu et al., 2011), so the disappearance of La_2O_3 reflections and the apparent increase in the $LaFeO_3$ fraction are interpreted as a consequence of reduced diffracting volume and enhanced microstrain in the crystallites induced by milling. These effects are known to broaden diffraction peaks, reduce their intensity, and may render minor phases undetectable by XRD (Suryanarayana, 2001). Similar behavior has been reported in mechanically milled La–Fe oxide systems, where progressive peak broadening and intensity reduction of La-containing precursor phases were associated with particle refinement (Sorescu et al., 2011).

Mössbauer
Room-temperature Mössbauer spectra of samples ATLFO5 and LFO5 are presented in Figure 4. In both cases, the data are well reproduced by a single Lorentzian sextet, whose hyperfine parameters, obtained from the fits, are summarized in Table 3.

Figure 4

Mössbauer spectrum of samples (a) ATLFO5 and (b) LFO5 at 300 K. Blue points are the measurements and the black line is the fit. The difference between the experimental and the fit is shown below the graph.

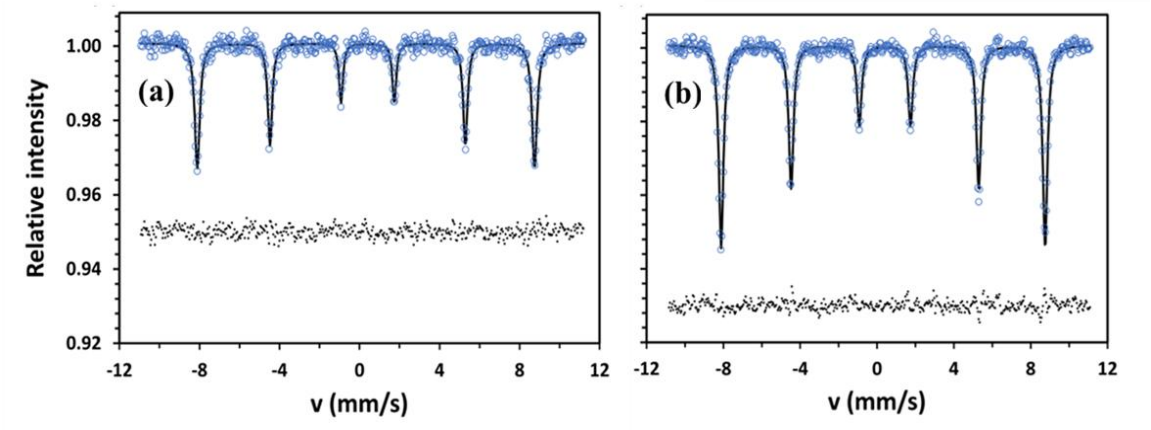

Table 3

Calculated hyperfine parameters obtained for samples ATLFO5 and LFO5. All parameters are given relative to metallic α-Fe.

Sample	Site	δ (mm/s)	ϵ (mm/s)	B_{hf} (T)	Γ (mm/s)	Population (%)	χ^2
ATLFO5	Sextet	0.36(5)	−0.04(5)	52.28(4)	0.24(4)	100	0.56
LFO5	Sextet	0.36(3)	−0.04(3)	52.31(2)	0.26(4)	100	0.76

These values match well with those reported for $LaFeO_3$ in the literature (Acosta et al., 2023; Al-Mamari et al., 2024; Lakshamana et al., 2019; Saha et al., 2020; Scrimshire et al., 2018). Both ATLFO5 and LFO5 show virtually identical isomer shifts ($\delta \approx 0.36$ mm/s), small quadrupole shifts ($\epsilon \approx -0.04$ mm/s), and large hyperfine fields ($B_{hf} \approx 52.3$ T) associated with the antiferromagnetic (AFM) coupling of $LaFeO_3$. These values differ from those of hematite, which typically exhibits a larger quadrupole shift ($\epsilon \approx -0.21$ mm/s) and a slightly smaller hyperfine field ($B_{hf} \approx 51.7$ T) (Zboril et al., 2002).

Despite the presence of a hematite secondary phase detected by XRD in both samples, no additional Mössbauer components can be resolved at room temperature. The dominance of the $LaFeO_3$ sextet indicates that the magnetic contribution of hematite, if present, is too weak to produce a distinct sub-spectrum, likely due to its low fraction. Attempts to fit a

second sextet in both samples did not improve the statistical quality of the fit, despite the slight asymmetry observed in some of its outer lines.

It can be remarked, as seen in Figure 4, that the relative intensity of the $LaFeO_3$ Mössbauer component is lower in ATLFO5 compared to LFO5. This suggests a lower effective contribution of resonant Fe nuclei associated with the $LaFeO_3$ phase (Dickson & Berry, 2005), which may be related to the presence of impurities and/or non-reacted phases in the sample obtained from the green precursor.

Chemical composition and morphology

FTIR

FTIR measurements were performed to analyze the chemical composition of the obtained samples. Figure 5 presents the FTIR spectra of samples ATLFO5 and LFO5. Since the spectra were acquired under different measurement conditions, a direct comparison of position band intensities is not intended. In ATR-FTIR, it is quite common to observe shifts in some bands compared to transmitted FTIR. This occurs due to differences in the physical mechanism of radiation-sample interaction, the penetration depth of the evanescent wave, and scattering/refraction effects. In oxides, typical shifts range from a few cm^{-1} to ~30 cm^{-1}, depending on the instrument, the ATR crystal, the preparation, and the particle size (Colthup et al., 1990; Griffiths & de Haseth, 2007; Salzer & Siesler, 2009). The analysis is thus restricted to identifying characteristic vibrational features.

The LFO5 spectrum exhibits a simple and clean profile, dominated solely by two characteristic bands located around 403 and 534 cm^{-1}, associated with La–O–La, Fe–O–Fe, and Fe–O/La–O vibration modes characteristic of the perovskite structure of $LaFeO_3$ (Deng et al., 2019; Ozkan et al., 2020; Thuy & Minh, 2012; Vijayaraghavan et al., 2017). The ATLFO5 spectrum shows a slight blue shift of the Fe–O/La–O vibrational band, still within the range reported for samples synthesized from organic precursors "(Ozkan, et al., 2020)". Additionally, weak features are observed that can be attributed to residual species derived from tannic acid, including bands near 3430 cm^{-1} (phenolic O–H or adsorbed water), ~2926 cm^{-1} (C–H stretching), ~1630 cm^{-1} (H–O–H bending), and ~1384 cm^{-1} (COO^- stretching) (Freire et al., 2023; Cherkezova-Zheleva et al., 2014; Vijayaraghavan et al., 2017, Pirtarighat et al., 2019; Barnawi et al., 2022; Ahmad et al., 2013; Radzikowska-Buchner et al., 2023). Despite their low intensity, the presence of these bands suggests that traces of precursor-derived species may remain after calcination.

Figure 5

FTIR spectrum of samples ATLFO5 (red) and LFO5 (blue)

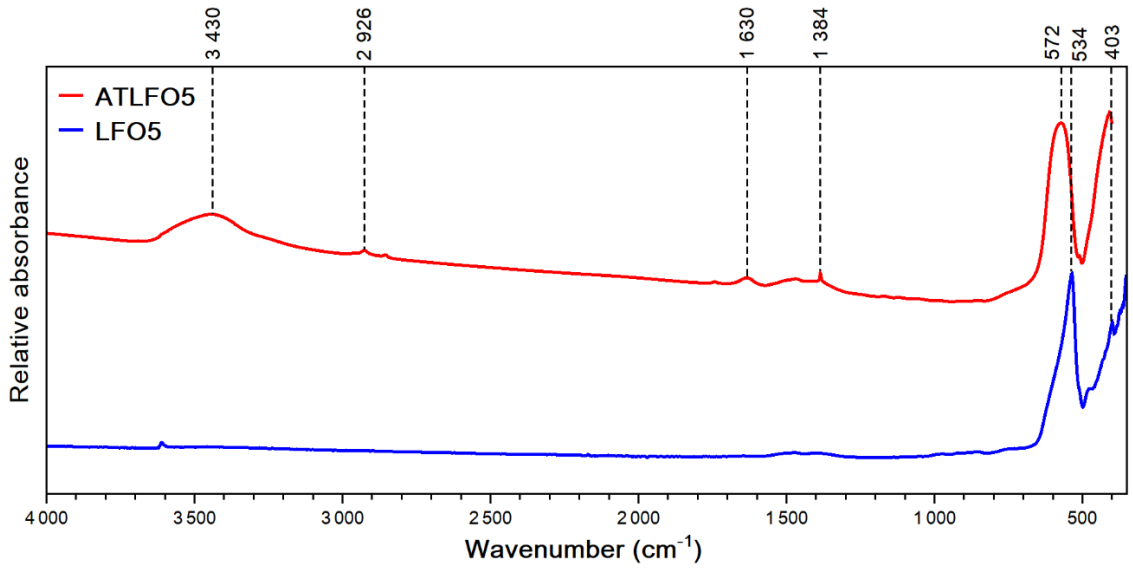

XPS

XPS measurements were performed to characterize the surface chemical states of sample ATLFO5. The analysis focused on ATLFO5 due to the residual species identified by FTIR and XRD in this sample. Figure 6 shows the survey spectrum of ATLFO5.

Figure 6

XPS survey spectrum of sample ATLFO5.

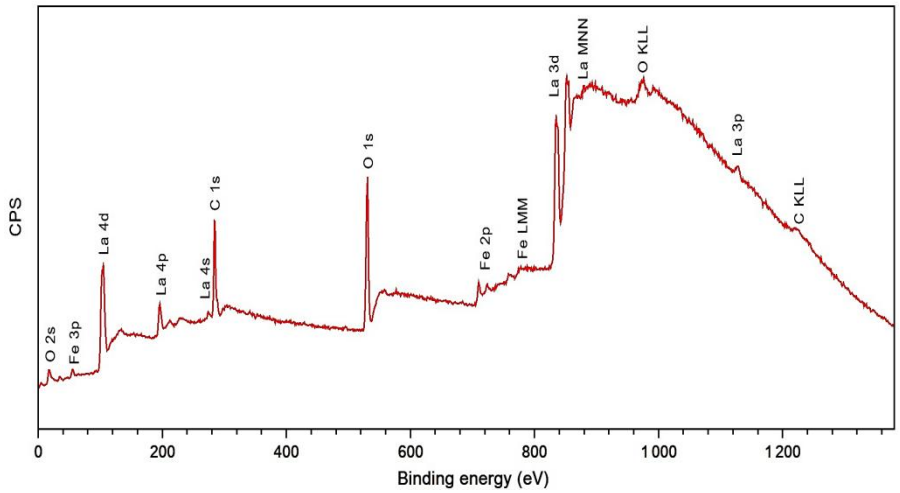

A first notable feature is the comparatively intense C 1s signal, which appears stronger than what is typically reported for $LaFeO_3$ prepared through other routes (Das et al., 2024; Ozkan et

al., 2020), where this line is usually attributed to adventitious carbon. To clarify the origin of this enhanced contribution, the high-resolution C 1s, O 1s, La 3d and Fe 2p spectra were examined in detail. The fitted spectra are presented in Figure 7.

Figure 7

Fitted high-resolution spectra of lines (a) C1s, (b) O1s, (c) La3d, and (d) Fe2p in sample ATLFO5.

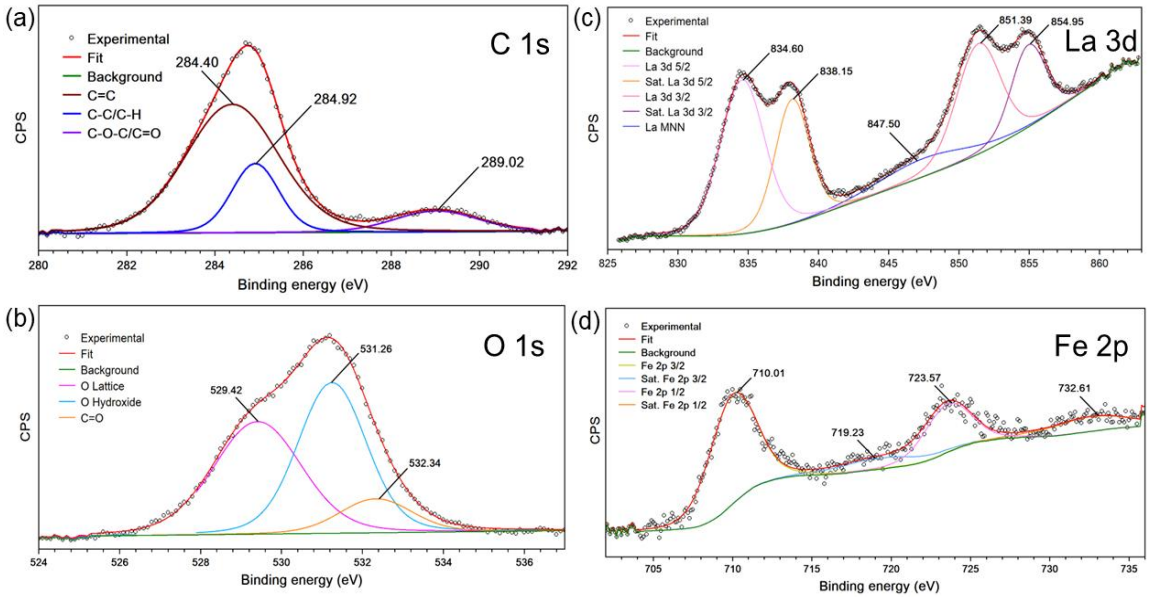

The C 1s envelope (Figure 7a) can be deconvoluted into three components at approximately 284.4, 284.9, and 289.0 eV. The lowest-energy component is characteristic of aromatic C=C environments, the peak at ~284.9 eV corresponds to typical adventitious C–C/C–H species, and the component at ~289.0 eV lies within the binding-energy range of carbonyl-type groups (C=O or O–C=O) (Beamson & Briggs, 1992).

The O 1s spectrum of ATLFO5 can be deconvoluted into three components: a dominant peak at ~529.4 eV corresponding to lattice oxygen in $LaFeO_3$, a contribution at ~531.3 eV associated with surface hydroxyl groups, and a higher-binding-energy component at ~532.2–533.0 eV attributable to oxygen in C–O and C=O environments. The consistency between the C 1s and O 1s envelopes indicates the presence of residual carbon-containing species on the surface after calcination. Although XPS probes only the outermost few nanometers, these surface features suggest that organic-derived species were not completely removed and may have locally reduced the effective contact between La_2O_3 and Fe_2O_3 particles during calcination. Such an effect could contribute to incomplete reaction in some regions, thereby

explaining the lower phase purity observed for ATLFO compared to LFO.

The La 3d spectrum (Figure 7c) exhibits the characteristic La^{3+} doublet, with La $3d_{5/2}$ and La $3d_{3/2}$ peaks at ~834.5 and ~851.5 eV, accompanied by their corresponding satellite features at ~838 and ~855 eV characteristic of the presence of species of La^{3+} on the surface of the material (Deng et al., 2019; Ozkan et al., 2020). A weak La MNN Auger contribution is also visible near ~847–848 eV.

The Fe 2p region (Figure 7d) displays Fe 2p3/2 and Fe 2p1/2 components at ~710.0 and ~723.6 eV, characteristic of Fe3+ species (Deng et al., 2019), along with satellite features around ~719 and ~733 eV. No additional components attributable to Fe^{2+} or mixed-valence states are detected.

A slight shift of the Fe $2p_{1/2}$ peak with respect to typical $LaFeO_3$ values (Ozkan et al., 2020; Das et al., 2024) may reflect the contribution of the minor hematite phase identified by XRD.

SEM

SEM was used to examine the morphology and particle-size distribution of the calcined powders. Figure 8 shows representative micrographs of the ATLFO5 sample.

The material exhibits a relatively homogeneous morphology composed of micrometer-scale agglomerates and smaller, isolated particles, many of which are spherical or slightly spheroidal. A particle-size analysis carried out in region b (Figure 9) shows a distribution spanning approximately 40–200 nm, with the highest concentration between 60 and 140 nm. Fitting the histogram with a log-normal function yields an average particle size of 107.5 nm and a positively skewed (1,11) distribution.

Figure 8
Two different regions of sample (a,c) ATLFO5 and (b,d) their corresponding magnified views.

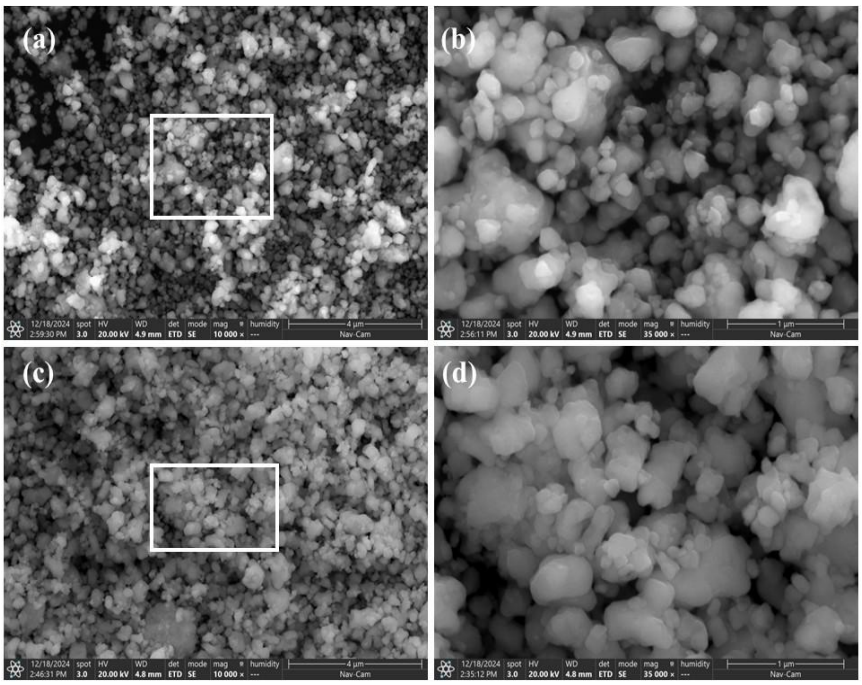

Figure 9
Particle length histogram of region b in Figure 8 in sample ATLFO5.

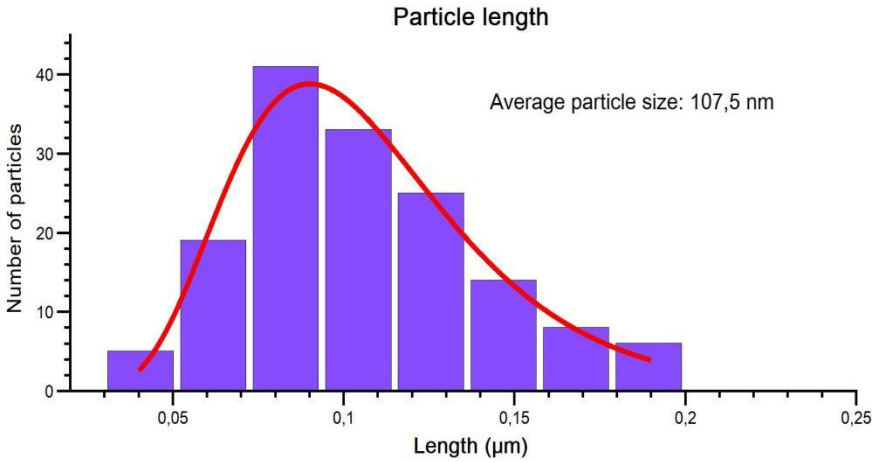

Figure 10 presents micrographs of LFO5, synthesized from commercial precursors. Its morphology is broadly similar to that of ATLFO5, but the particle-size distribution obtained from region d (Figure 11) is shifted toward larger sizes, ranging from 60 to 240 nm with an average of 126.1 nm and a slightly smaller positive skewness (0,974).

Figure 10

Two different regions of sample (a,c) LFO5 and (b,d) their corresponding magnified views.

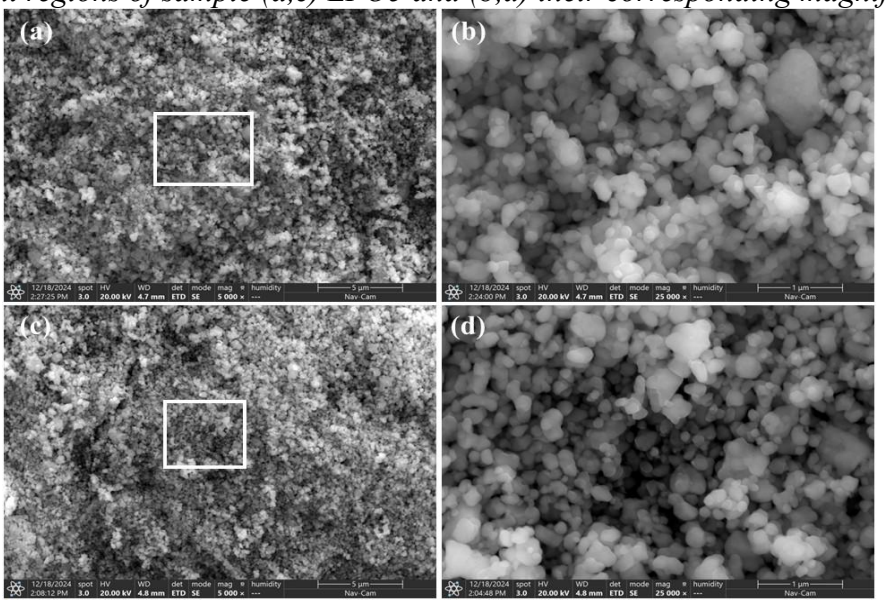

Since $LaFeO_3$ formation has been proposed to occur mainly through the diffusion of La^{3+} into the Fe_2O_3 lattice (Sorescu et al., 2011), this size difference is likely related to the different grain sizes of the hematite precursors, since the tannic acid-derived hematite is known to be finer (Freire et al., 2023) than the commercial one.

Figure 11

Particle length histogram of region d in Figure 10 in sample LFO5.

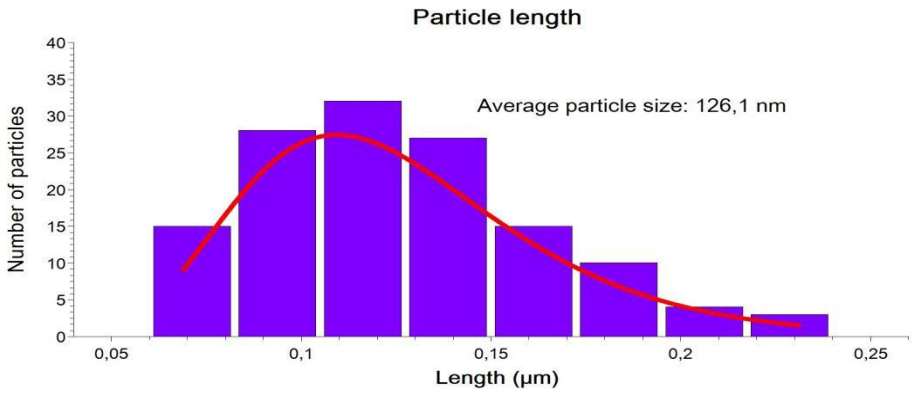

Magnetic measurements

To study the magnetic properties of the synthesized samples, Figure 12 shows the room-temperature M–H curves of samples ATLFO5 and LFO5.

Figure 12

Hysteresis loop at 300 K of samples ATLFO5 (red) and LFO5 (black). Inset is the magnified hysteresis loop.

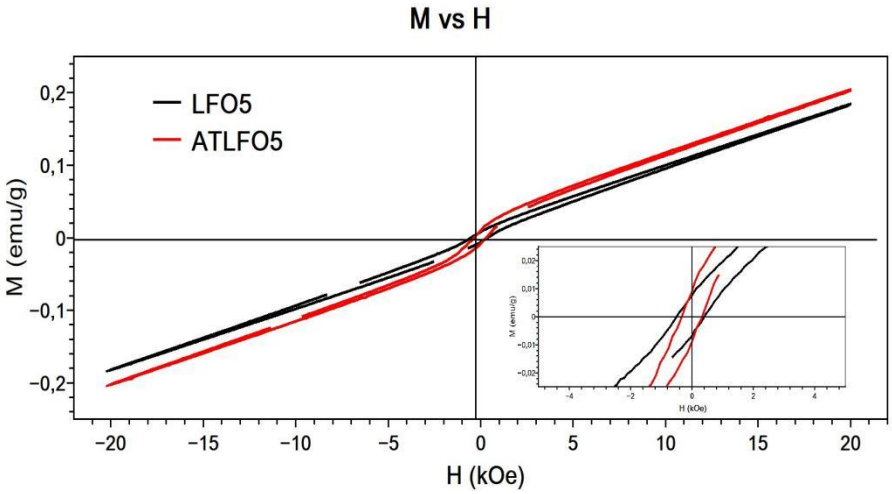

Neither sample reaches magnetic saturation within the ±20 kOe range; instead, it shows a nearly linear dependence characteristic of the AFM ordering in $LaFeO_3$. The enlarged view near the origin reveals a small but finite remanent magnetization in both cases, indicating a weak ferromagnetic (WF) component. This behavior is consistent with the spin canting commonly reported in distorted orthoferrites (Abbas et al., 2018; Jain & Srivastava, 2016; Kundu et al., 2019; Popa & Moreno, 2010; Thuy & Minh, 2012).

Table 4

Remanent magnetization (M_r) and coercive field (H_c) for samples ATLFO5 and LFO5

Parameter	ATLFO5	LFO5
[1]M_r (emu/g)	0.008886	0.007458
[1]H_c (Oe)	325	495

[1]Values obtained from linear interpolation of the hysteresis data. The uncertainties are $\Delta Mr \approx \pm 3 \times 10 - 6$ emu/g and $\Delta H \approx \pm 1$ Oe.

The overall magnetization is higher in ATLFO5 than in LFO5, a difference that can reasonably be attributed to microstructural factors. ATLFO5 contains a larger fraction of smaller particles, increasing the contribution of uncompensated surface spins, which are more easily aligned by the external field. Although both samples were subjected to dry milling, differences in the resulting surface disorder or defect density, combined with their distinct grain-size distributions, may also influence the magnetic response. Within this framework, ATLFO5 exhibits the largest magnetization because it combines a greater surface-to-volume ratio with defects-induced contributions associated with milling. The remanent magnetization values obtained by linear interpolation (Table 4) follow this trend, with ATLFO5 showing the highest M_r and LFO5 a slightly lower value.

The coercive fields show relative low values, and differ between the soft behavior (Guimarães, 2017), differ between the two samples, with LFO5 exhibiting a higher coercivity (~495 Oe) than ATLFO5 (~325 Oe). Since both materials underwent identical post-milling conditions, this difference is primarily attributed to their distinct grain-size distributions. In $LaFeO_3$, coercivity is known to depend on grain size and to reach a maximum at intermediate dimensions, around ~125 nm (Koferstein et al., 2013). The particle-size distribution of LFO5 lies closer to this regime, whereas ATLFO5 contains a larger fraction of finer particles, resulting in a lower effective coercivity.

Figure 13 shows the ZFC and FC magnetization curves of samples ATLFO5 and LFO5. Both materials show a magnetic transition at ~260 K, a feature that is not expected for pure $LaFeO_3$ but is fully consistent with the Morin transition of the minor Fe_2O_3 phase detected by XRD (Ozdemir et al., 2008). The transition is noticeably sharper in LFO5, which can be attributed to the larger fraction of particles above the nanometric regime (>100 nm). In contrast, ATLFO5 exhibits a more diffuse transition, which can be associated with its larger fraction of nanoparticles. As particle size decreases, the surface-to-volume ratio increases and surface effects progressively dominate the magnetic anisotropy landscape, leading to a distribution of anisotropy energies (Kodama, 1999). This distribution spreads the Morin transition over a finite temperature range, producing the gradual behavior observed experimentally.

Figure 13

ZFC and FC curves of samples ATLFO5 (orange and blue) and LFO5 (green and purple)

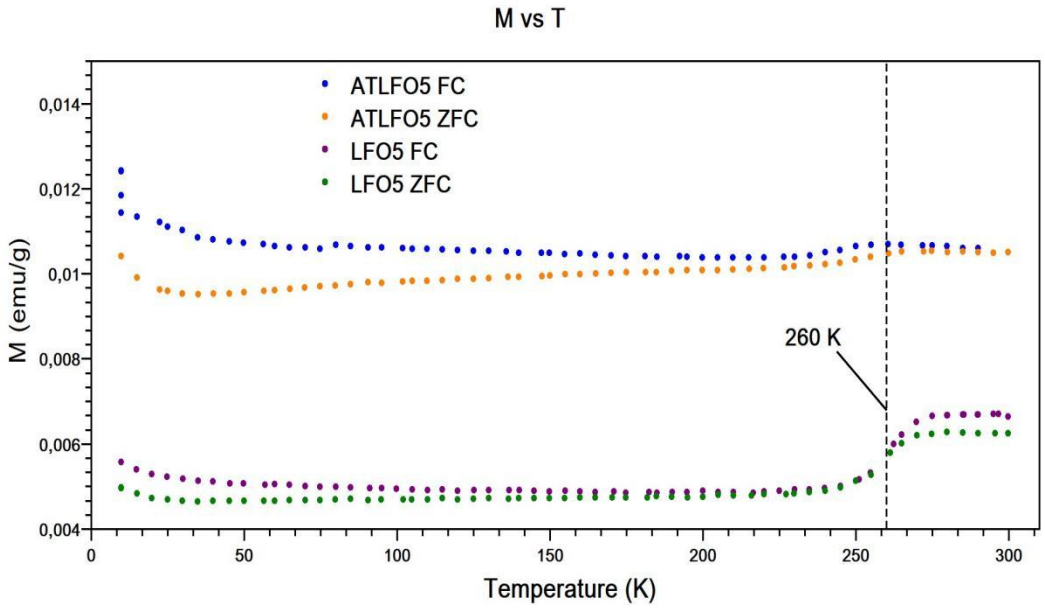

A pronounced bifurcation between ZFC and FC curves is observed in both samples, beginning near room temperature, indicating strong thermal irreversibility. Upon cooling, the FC magnetization increases while the ZFC response remains significantly lower, a behavior commonly associated with uncompensated or weakly pinned spins. This effect is frequently interpreted within frameworks where surface regions contribute additional anisotropy and metastable spin configurations (Koferstein et al., 2013; Al-Mamari et al, 2024). In our materials, the presence of nanometric grains, together with the structural disorder induced by the dry milling step, enhances these contributions by introducing strain, defects, and locally frustrated exchange interactions.

As the temperature increases from the low-T region in ZFC, thermal activation gradually unblocks the surface spins, producing the expected rise in magnetization (Al-Mamari et al., 2024). A clear maximum cannot be identified because the Morin transition of the secondary Fe_2O_3 phase overlaps with this regime, and the ZFC–FC separation remains small but still observable above ~ 255 K.

CONCLUSIONS

$LaFeO_3$ perovskite was successfully synthesized by a low-energy solid-state route using both commercial hematite and hematite derived from tannic acid as iron precursors. Although all samples crystallized predominantly in the orthorhombic $LaFeO_3$ phase, clear differences in phase formation, microstructure and magnetic response were observed depending on the nature of the precursor.

The use of tannic acid–derived hematite led to a less complete solid-state reaction after calcination, as evidenced by the presence of residual La_2O_3 and a lower $LaFeO_3$ phase fraction compared to samples synthesized from commercial hematite. FTIR and XPS analyses revealed that organic-derived species persist in the green-precursor samples even after calcination at 800 °C. These residual carbonaceous species are proposed to hinder cation diffusion during calcination, slowing the formation of $LaFeO_3$ and resulting in a more heterogeneous reaction pathway.

Post-calcination milling increased microstrain and reduced crystallite size in all samples without significantly altering lattice parameters, confirming the structural robustness of the $LaFeO_3$ unit cell. However, the effect was more pronounced in the green-precursor material, which exhibited smaller crystallites and higher microstrain. This enhanced susceptibility to mechanical refinement is attributed to its initially heterogeneous and multiphasic microstructure, containing a larger density of internal interfaces that act as mechanically weak regions.

Magnetic measurements showed that all samples display antiferromagnetic behavior with a weak-ferromagnetic component at room temperature. The higher magnetization observed in the green-precursor sample after milling is consistently explained by its smaller particle size and increased surface-to-volume ratio, which enhances the contribution of uncompensated surface spins. ZFC–FC measurements further revealed a Morin transition associated with the minor hematite phase and strong thermal irreversibility, particularly pronounced in samples containing a higher fraction of nanometric grains.

Overall, this work demonstrates the viability of tannic acid as a bio-derived precursor in the solid-state synthesis of $LaFeO_3$, but at the cost of introducing persistent carbonaceous species that limit reaction completeness under mild thermal conditions. While this limits phase purity, it simultaneously promotes finer microstructures and enhanced magnetic response after mechanical refinement.

BIBLIOGRAPHIC REFERENCES

Abbas, Y. M., Mansour, A. B., Ali, S. E. M., & Abdel-Hamid, A. H. I. (2018). Synthesis, structure and magnetic characterization of orthoferrite $LaFeO_3$ nanoparticles. *Journal of Advances in Physics, 14*(3), 5664–5681. https://doi.org/10.24297/jap.v14i3.7693

Acosta, H., López, C. A., Furlong, O. J., Nazzarro, M. S., Marchetti, S. G., Cadús, L. E., & Agüero, F. N. (2023). Highly resistant $LaCo_{1-x}Fe_xO_3$ perovskites used in chlorobenzene catalytic combustion. *Catalysts, 13*(1), 42. https://doi.org/10.3390/catal13010042

Ahmad, T. (2014). Reviewing the tannic acid mediated synthesis of metal nanoparticles. *Journal of Nanotechnology, 2014*, 1–11. https://doi.org/10.1155/2014/954206

Ahmad, T., Wani, I. A., Manzoor, N., Ahmed, J., & Asiri, A. M. (2013). Biosynthesis, structural characterization and antimicrobial activity of gold and silver nanoparticles. *Colloids and Surfaces B: Biointerfaces, 107*, 227–234. https://doi.org/10.1016/j.colsurfb.2013.02.004

Al-Mamari, R. T., Widatallah, H. M., Elzain, M. E., Gismelseed, A. M., Al-Rawas, A. D., Al-Harthi, S. H., Myint, M. T. Z., Al-Saqri, N., & Al-Abri, M. (2024). Core and surface structure and magnetic properties of mechano-synthesized $LaFeO_3$ nanoparticles and their Eu^{3+}-doped and Eu^{3+}/Cr^{3+}-co-doped variants. *Scientific Reports, 14*(1). https://doi.org/10.1038/s41598-024-65757-z

Arjun, N., Pan, G., & Yang, T. C. (2017). The exploration of lanthanum based perovskites and their complementary electrolytes for the supercapacitor applications. *Results in Physics, 7*, 920–926. https://doi.org/10.1016/j.rinp.2017.02.013

Azouzi, W., Sigle, W., Labrim, H., & Benaissa, M. (2019). Sol-gel synthesis of nanoporous $LaFeO^3$ powders for solar applications. *Materials Science in Semiconductor Processing, 104*, 104682. https://doi.org/10.1016/j.mssp.2019.104682

Barnawi, N., Allehyani, S., & Seoudi, R. (2022). Biosynthesis and characterization of gold nanoparticles and its application in eliminating nickel from water. *Journal of Materials Research and Technology, 17*, 537–545. https://doi.org/10.1016/j.jmrt.2021.12.013

Beamson, G., & Briggs, D. (1992). *High resolution XPS of organic polymers: The Scienta ESCA300 database*. Wiley.

Berbenni, V., Bruni, G., Milanese, C., Girella, A., & Marini, A. (2018). Synthesis and characterization of $LaFeO_3$ powders prepared by a mixed mechanical/thermal

processing route. *Journal of Thermal Analysis and Calorimetry, 133*(1), 413–419. https://doi.org/10.1007/s10973-017-6878-z

Cherkezova-Zheleva, Z., Paneva, D., Yordanova, I., Shopska, M., & Kolev, H. (2014). Mechanochemical preparation and properties of nanodimensional perovskite materials.

Acta Physica Polonica A, 126(4), 916–920. https://doi.org/10.12693/aphyspola.126.916

Choi, J., Kim, B., Song, S., & Park, J. (2016). A composite cathode with undoped $LaFeO_3$ for protonic ceramic fuel cells. *International Journal of Hydrogen Energy, 41*(22), 9619–9626. https://doi.org/10.1016/j.ijhydene.2016.03.115

Colthup, N. B., Daly, L. H., & Wiberley, S. E. (1990). *Introduction to infrared and Raman spectroscopy* (3rd ed.). Academic Press.

Cristóbal, A., Botta, P., Bercoff, P., & López, J. P. (2009). Mechanosynthesis and magnetic properties of nanocrystalline $LaFeO_3$ using different iron oxides. *Materials Research Bulletin, 44*(5), 1036–1040. https://doi.org/10.1016/j.materresbull.2008.11.015

Das, S., Das, S., Bajorek, A., & Chakrabarti, P. K. (2024). Enhanced magnetic behavior of $LaFeO_3$ by co-doping with Nd^{3+} and V^{5+} substitution ($La_{0.8}Nd_{0.2}Fe_{0.95}V_{0.05}O_3$). *Journal of Magnetism and Magnetic Materials, 606*, 172333. https://doi.org/10.1016/j.jmmm.2024.172333

Deng, H., Mao, Z., Xu, H., Zhang, L., Zhong, Y., & Sui, X. (2019). Synthesis of fibrous $LaFeO_3$ perovskite oxide for adsorption of Rhodamine B. *Ecotoxicology and Environmental Safety, 168*, 35–44. https://doi.org/10.1016/j.ecoenv.2018.09.056

Dickson, D. P. E., & Berry, F. J. (1986). *Mössbauer spectroscopy*. Cambridge University Press.

Finlay, C., Gunawan, G., Biris, A. S., Bourdo, S., Kunets, V., Salamo, G., & Viswanathan, T. (2012). Novel microwave-assisted synthesis of renewable-resource based carbon-magnetite nanocomposites. *Journal of Wood Chemistry and Technology, 32*(3), 268–278. https://doi.org/10.1080/02773813.2012.659320

Freire, A., Chung, E., Mendoza, I., & Jaén, J. A. (2023). Green synthesis of iron oxide nanoparticles using *Caesalpinia coriaria* (Jacq.) Willd. fruits extract. *Hyperfine Interactions, 244*(1). https://doi.org/10.1007/s10751-023-01817-6

Griffiths, P. R., & de Haseth, J. A. (2007). *Fourier transform infrared spectrometry* (2nd ed.). Wiley.

Guimarães, A. P. (2017). *Principles of nanomagnetism*. In *Nanoscience and technology*. https://doi.org/10.1007/978-3-319-59409-5

Herrera-Becerra, R., Rius, J. L., & Zorrilla, C. (2010). Tannin biosynthesis of iron oxide nanoparticles. *Applied Physics A, 100*(2), 453–459. https://doi.org/10.1007/s00339-010-5903-x

Jadhav, A., Gaikwad, A., Samuel, V., & Ravi, V. (2006). A low temperature route to prepare $LaFeO_3$ and $LaCoO_3$. *Materials Letters, 61*(10), 2030–2032. https://doi.org/10.1016/j.matlet.2006.08.009

Jaén, J. A., Higuera, F., Gil, O., Chung, E., & Caballero-Manrique, G. (2026). Synthesis and characterisation of perovskite-type $LaFeO_3$ using solid-state reaction assisted by low-energy ball milling. *Interactions, 247*(1). https://doi.org/10.1007/s10751-026-02434-9

Jain, P., & Srivastava, S. (2016). Structural investigation and zero-field-cooled exchange bias in nanocrystalline $LaFeO_3$. *Journal of Superconductivity and Novel Magnetism, 29*(8), 2089–2097. https://doi.org/10.1007/s10948-016-3520-4

Keav, S., Matam, S., Ferri, D., & Weidenkaff, A. (2014). Structured perovskite-based catalysts and their application as three-way catalytic converters—A review. *Catalysts, 4*(3), 226–255. https://doi.org/10.3390/catal4030226

Kodama, R. (1999). Magnetic nanoparticles. *Journal of Magnetism and Magnetic Materials, 200*(1–3), 359–372. https://doi.org/10.1016/S0304-8853(99)00347-9

Koferstein, R., Jäger, L., & Ebbinghaus, S. G. (2013). Magnetic and optical investigations on $LaFeO_3$ powders with different particle sizes and corresponding ceramics. *Solid State Ionics, 249–250*, 1–5. https://doi.org/10.1016/j.ssi.2013.07.001

Kucharczyk, B., Winiarski, J., Szczygieł, I., & Adamska, K. (2020). Physicochemical properties of $LaFeO_3$ perovskite prepared by various methods and its activity in the oxidation of hydrocarbons. *Industrial & Engineering Chemistry Research, 59*(38), 16603–16613. https://doi.org/10.1021/acs.iecr.0c03035

Kuhn, J., & Ozkan, U. (2007). Surface properties of Sr^- and Co-doped $LaFeO_3$. *Journal of Catalysis, 253*(1), 200–211. https://doi.org/10.1016/j.jcat.2007.10.005

Kundara, R., & Baghel, S. (2024). Performance analysis of $LaFeO_3$ perovskite solar cells: A theoretical and experimental study. *Solid State Communications, 389*, 115590. https://doi.org/10.1016/j.ssc.2024.115590

Kundu, S. K., Rana, D. K., Karmakar, L., Das, D., & Basu, S. (2019). Enhanced multiferroic, magnetodielectric and electrical properties of Sm doped lanthanum ferrite nanoparticles. *Journal of Materials Science: Materials in Electronics, 30*(11), 10694–10710. https://doi.org/10.1007/s10854-019-01415-9

Lakshamana, T., Pradhan, M. K., Chandrasekhar, M., Ramakrishna, P. V., & Dash, S. (2019). Structural, magnetic, grain and grain boundary mediated conduction features of low dimensional $LaFeO_3$ nanoparticles. *Journal of Physics: Condensed Matter, 31*(34), 345803. https://doi.org/10.1088/1361-648X/ab20a3

Lakshminarayanan, N., Kuhn, J. N., Rykov, S. A., Millet, J. M., & Ozkan, U. S. (2010). Doped $LaFeO_3$ as SOFC catalysts: Control of oxygen mobility and oxidation activity. *Catalysis Today, 157*(1–4), 446–450. https://doi.org/10.1016/j.cattod.2010.03.037

Lebid, M., & Omari, M. (2014). Synthesis and electrochemical properties of $LaFeO_3$ oxides prepared via sol–gel method. *Arabian Journal for Science and Engineering, 39*(1), 147–152. https://doi.org/10.1007/s13369-013-0883-8

Li, F., Wang, Z., Wang, A., Wu, S., & Zhang, L. (2020). N-type $LaFe_{1-x}Mn_xO3$ prepared by sol-gel method for gas sensing. *Journal of Alloys and Compounds, 816*, 152647. https://doi.org/10.1016/j.jallcom.2019.152647

Liu, X., Ji, H., Gu, Y., & Xu, M. (2006). Preparation and acetone sensitive characteristics of nano-$LaFeO_3$ semiconductor thin films by polymerization complex method. *Materials Science and Engineering B, 133*(1–3), 98–101. https://doi.org/10.1016/j.mseb.2006.06.027

Lugo, L. I. O., Miró, A. M. B., Luévanos, A. M., Escobedo, C. A. C., Cardona, M. R., & Jesús, F. S. (2021). Multiferroicidad en $LaFeO_3$ sintetizada mediante molienda de alta energía. *Tópicos de Investigación en Ciencias de la Tierra y Materiales, 8*(8), 20–24. https://doi.org/10.29057/aactm.v8i8.7586

Mawdsley, J. R., & Krause, T. R. (2007). Rare earth-first-row transition metal perovskites as catalysts for the autothermal reforming of hydrocarbon fuels to generate hydrogen. *Applied Catalysis A: General, 334*(1–2), 311–320. https://doi.org/10.1016/j.apcata.2007.10.018

Moghadam, L. N., & Ranjbar, Z. R. (2019). Cost-efficient solar cells using nanocrystalline perovskite La (Fe and Mn) O_3 and candle soot: Theory and experiment. *Journal of Alloys and Compounds, 785*, 117–124. https://doi.org/10.1016/j.jallcom.2019.01.068

Morales, L., Sierra-Gallego, G., Barrero, C., & Arnache, O. (2016). Relative recoilless F-factors in $REFeO_3$ (RE = rare-earth La, Pr, Nd and Sm) orthoferrites synthesized by self-combustion method. *Materials Science and Engineering B, 211*, 94–100. https://doi.org/10.1016/j.mseb.2016.06.005

Naibaho, M., Widakdo, J., Kurniawan, B., Nehan, P. Z. Z., Vitayaya, O., Novita, Ramlan, Adi, W. A., & Ginting, M. (2024). Analysis of structure, morphology, magnetic properties, and microwave absorption of lanthanum orthoferrite ($LaFeO_3$). *Science & Technology Indonesia, 9*(4), 851–856. https://doi.org/10.26554/sti.2024.9.4.851-856

Ozkan, D. Ç., Turk, A., & Çelik, E. (2020). Synthesis and characterizations of sol–gel derived $LaFeO_3$ perovskite powders. *Journal of Materials Science: Materials in Electronics, 31*(24), 22789–22809. https://doi.org/10.1007/s10854-020-04803-8

Ozdemir, O., Dunlop, D. J., & Berquó, T. S. (2008). Morin transition in hematite: Size dependence and thermal hysteresis. *Geochemistry, Geophysics, Geosystems, 9*(10). https://doi.org/10.1029/2008gc002110

Pasieczna-Patkowska, S., Cichy, M., & Flieger, J. (2025). Application of Fourier transform infrared (FTIR) spectroscopy in characterization of green synthesized nanoparticles. *Molecules, 30*(3), 684. https://doi.org/10.3390/molecules30030684

Pérez, H. A., López, C. A., Furlong, O. J., Nazzarro, M. S., Marchetti, S. G., Cadús, L. E., & Agüero, F. N. (2022). Highly resistant $LaCo_{1-x}Fe_xO_3$ perovskites used in chlorobenzene catalytic combustion. *Catalysts, 13*(1), 42. https://doi.org/10.3390/catal13010042

Pirtarighat, S., Ghannadnia, M., & Baghshahi, S. (2018). Green synthesis of silver nanoparticles using the plant extract of *Salvia spinosa* grown in vitro and their antibacterial activity assessment. *Journal of Nanostructure in Chemistry, 9*(1), 1–9. https://doi.org/10.1007/s40097-018-0291-4

Popa, M., & Moreno, J. M. C. (2010). Lanthanum ferrite ferromagnetic nanocrystallites by a polymeric precursor route. *Journal of Alloys and Compounds, 509*(10), 4108–4116. https://doi.org/10.1016/j.jallcom.2010.12.162

Prasad, P., Sivanandan, V. T., & Prasad, A. S. (2024). Room temperature ferromagnetic behavior of nanocrystalline $LaFeO_3$ perovskite oxide synthesized through phytochemical mediated combustion technique. *Journal of Cluster Science, 35*(3), 929–940. https://doi.org/10.1007/s10876-023-02516-6

Radzikowska-Büchner, E., Flieger, W., Pasieczna-Patkowska, S., Franus, W., Panek, R., Korona-Głowniak, I., Suśniak, K., Rajtar, B., Świątek, Ł., Żuk, N., Bogucka-Kocka, A., Makuch-Kocka, A., Maciejewski, R., & Flieger, J. (2023). Antimicrobial and apoptotic efficacy of plant-mediated silver nanoparticles. *Molecules, 28*(14), 5519. https://doi.org/10.3390/molecules28145519

Scrimshire, A., Lobera, A., Bell, A. M. T., Jones, A. H., Sterianou, I., Forder, S. D., & Bingham, P. A. (2018). Determination of Debye temperatures and Lamb–Mössbauer factors for $LnFeO_3$ orthoferrite perovskites (Ln = La, Nd, Sm, Eu, Gd). *Journal of Physics: Condensed Matter, 30*(10), 105704. https://doi.org/10.1088/1361-648X/aaab7d

Saha, J., Jana, Y., Mukherjee, G., Mondal, R., Kumar, S., & Gupta, H. (2020). Structure, Mössbauer spectroscopy and vibration phonon spectra in valence-bond force-field model approach for distorted perovskites $AFeO_3$ (A = La, Y). *Materials Chemistry and Physics, 240*, 122286. https://doi.org/10.1016/j.matchemphys.2019.122286

Salzer, R., & Siesler, H. W. (Eds.). (2009). *Infrared and Raman spectroscopic imaging*. Wiley-VCH.

Sorescu, M., Tianghon, X., & Hannan, A. (2011). Initial stage growth mechanism of $LaFeO_3$ perovskite through magnetomechanical ball-milling of lanthanum and iron oxides. *American Journal of Material Science, 1*(1), 57–66.
http://article.sapub.org/pdf/10.5923.j.materials.20110101.09.pdf

Sorescu, M., Xu, T., Burnett, J. D., & Aitken, J. A. (2011). Investigation of $LaFeO_3$ perovskite growth mechanism through mechanical ball milling of lanthanum and iron oxides. *Journal of Materials Science, 46*(20), 6709–6717. https://doi.org/10.1007/s10853-011-5625-2

Suryanarayana, C. (2001). Mechanical alloying and milling. *Progress in Materials Science, 46*(1–2), 1–184. https://doi.org/10.1016/S0079-6425(99)00010-9

Thuy, N. T., & Minh, D. L. (2012). Size effect on the structural and magnetic properties of nanosized perovskite $LaFeO_3$ prepared by different methods. *Advances in Materials Science and Engineering, 2012*, 1–6. https://doi.org/10.1155/2012/380306

Vijayaraghavan, T., Sivasubramanian, R., Hussain, S., & Ashok, A. (2017). A facile synthesis of $LaFeO_3$-based perovskites and their application towards sensing of neurotransmitters. *ChemistrySelect, 2*(20), 5570–5577. https://doi.org/10.1002/slct.201700723

Wang, B., Yu, Q., Zhang, S., Wang, T., Sun, P., Chuai, X., & Lu, G. (2017). Gas sensing with yolk-shell LaFeO3 microspheres prepared by facile hydrothermal synthesis. *Sensors And Actuators B Chemical*, *258*, 1215-1222. https://doi.org/10.1016/j.snb.2017.12.018

Zboril, R., Mashlan, M., & Petridis, D. (2002). Iron(III) oxides from thermal processes: Synthesis, structural and magnetic properties, Mössbauer spectroscopy characterization, and applications. *Chemistry of Materials, 14*(3), 969–982. https://doi.org/10.1021/cm0111074